

Experimental evidence for the influence of charge on the adsorption capacity of carbon dioxide on charged fullerenes

Stefan Ralser¹, Alexander Kaiser¹, Michael Probst¹, Johannes Postler¹, Michael Renzler¹,
Diethard K. Bohme^{2*} and Paul Scheier^{1*}

¹ Institut für Ionenphysik und Angewandte Physik, Leopold-Franzens-Universität Innsbruck,
Technikerstr. 25, 6020 Innsbruck, Austria.

² Department of Chemistry, York University, Toronto, ON, Canada M3J 1

*corresponding authors: Paul.Scheier@uibk.ac.at, dkbohme@yorku.ca

We show, with both experiment and theory, that adsorption of CO₂ is sensitive to charge on a capturing model carbonaceous surface. In the experiment we dope superfluid helium droplets with C₆₀ and CO₂ and expose them to ionising free electrons. Both positively and negatively charged C₆₀(CO₂)_n^{+/-} cluster ion distributions are observed with a high-resolution mass spectrometer and these show remarkable and reproducible anomalies in intensities that are strongly dependent on the charge. The highest adsorption capacity is seen with C₆₀⁺. Complementary density functional theory calculations and molecular dynamics simulations provided insight into the nature of the interaction of charged C₆₀ with CO₂ as well as trends in the packing of C₆₀⁺ and C₆₀⁻. The quadrupole moment of CO₂ itself was seen to be decisive in determining the charge dependence of the observed adsorption features. Our findings are expected to apply to adsorption of CO₂ by charged surfaces in general.

Introduction

The role of CO₂ as a greenhouse gas has provided a major driving force for experimental and theoretical studies of CO₂ adsorption and sequestration in mesoporous materials ¹, metal organic

frameworks and materials ^{2,3}, zeolites ^{4,5}, and polymer composite materials ⁶. Pristine and calcium-doped buckminsterfullerene ⁷ and various other carbonaceous materials also have been explored previously in this context, including graphites ^{8,9}, graphenes ¹⁰, nanotubes ¹¹⁻¹³ and carbon nanoscrolls ¹⁴. Density functional theory (DFT) has demonstrated that adsorption and also sequestration of CO₂ on boron nitride nanosurfaces can be strongly enhanced by surface charges ^{15, 16}. Trinh et al. studied charge dependent CO₂ adsorption in carbon mesopores by molecular dynamics simulations and also found enhanced selectivity for CO₂ adsorption compared to H₂ adsorption near artificially introduced surface charges ¹⁷. In a DFT study of nitrogen doped carbon nanotubes, Jiao et al. obtained a strong charge-dependence for CO₂ capture ¹⁸.

Here we have chosen buckminsterfullerene, C₆₀, as the carbonaceous adsorbate surface. We report the first experimental evidence for the influence of both positive and negative charge on the adsorption capacity of CO₂. We have extensive experience with experiments involving the adsorption of a variety of non-polar and some polar molecules on cationic C₆₀, C₇₀ and their aggregates at ultra-low temperatures (0.37 K) ¹⁹⁻²³. We have reported previously the mass spectrometric observation of remarkable anomalies in CO₂ coverage for the C₆₀ dimer and trimer cations (C₆₀)₂⁺ and (C₆₀)₃⁺ ²⁴. Here we track the adsorption of CO₂ on single C₆₀ cations and anions in the absence of steric constraints. Interesting and surprising anomalies are observed in this case as well, but we will show that these can be attributed to the unique electron distribution within the CO₂ molecule and its interaction with the charge on the C₆₀, and so provide new fundamental insights into the adsorption of carbon dioxide on charged carbonaceous surfaces.

The CO₂ molecule is roughly cylindrical and its quadrupole moment ($Q_a = -4.278 \text{ D } \text{\AA}^{25}$) corresponds to slightly negative terminal O atoms that can preferentially respond to a positive charge and to a slightly positive C atom that can preferentially respond to a negative charge on

isolated C_{60} ions. The CO_2 molecules will be vibrationally and rotationally cold at 0.37 K, the temperature of the helium droplet environment in which the adsorption takes place in our experiments.

Results and discussion

We exposed cold superfluid helium nanodroplets, doped with C_{60} and CO_2 , to electron ionization and then sampled the ions that are born within the helium nanodroplets and emerge upon droplet evaporation or ejection from the helium nanodroplets. The raw high-resolution mass-spectra of the cations and anions comprising $C_{60}(CO_2)_n^+$ and $C_{60}(CO_2)_n^-$, are shown in Figure 1. Several remarkable and reproducible features are evident from these spectra. The C_{60} cations and anions have the capacity to adsorb a very large number of CO_2 molecules within the superfluid helium droplets. Anomalously high intensity peaks emerge at specific values of n , viz. “magic numbers”, that imply special stabilities for these cluster ions. Furthermore, and even more remarkable, *the adsorption capacities of C_{60} cations and anions are different being higher for cations than anions*, as can be deduced from the tails of the shown mass spectra for high mass to charge ratio.

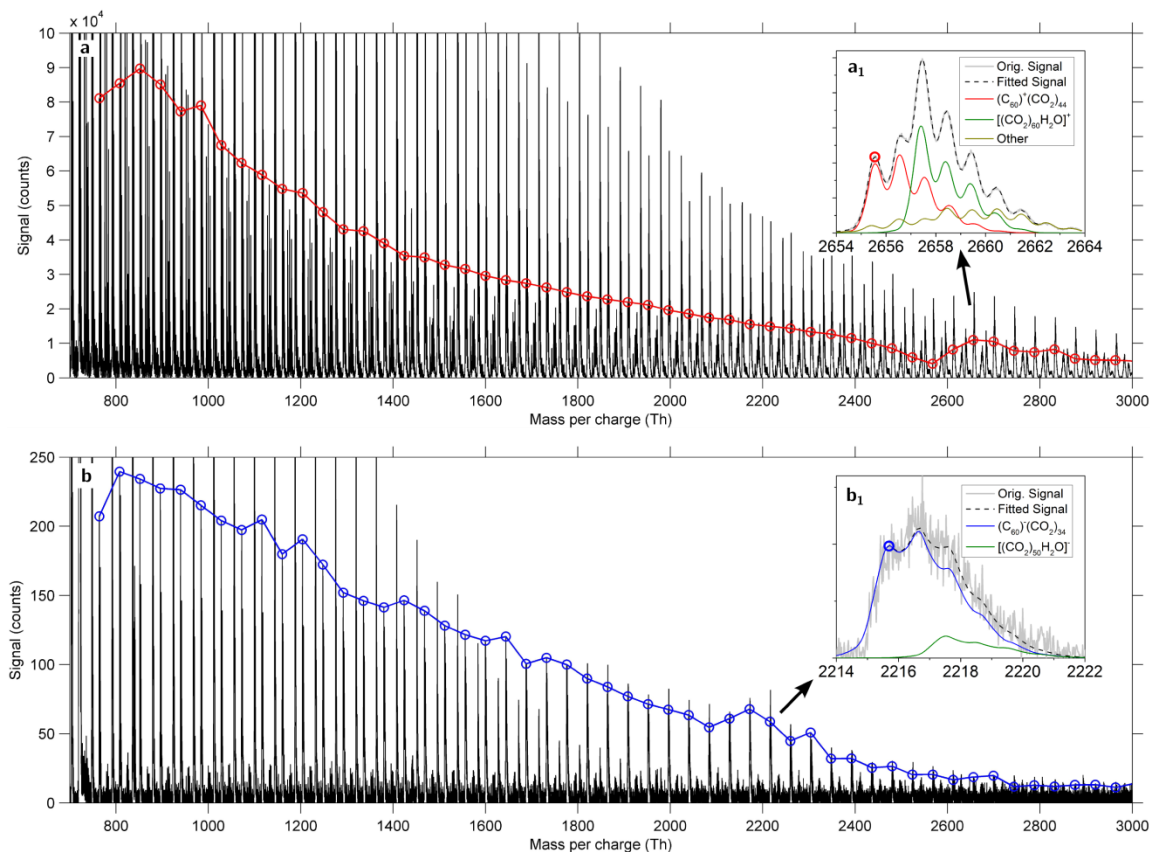


Figure 1: Raw mass spectrum for a) $(C_{60})^+(\text{CO}_2)_n$ and b) $(C_{60})^-(\text{CO}_2)_n$. The red and blue lines show the highest ion signal for the first isotopologue of the corresponding $C_{60}^\pm(\text{CO}_2)_n$ cluster. These data points are not corrected for contributions of other species that may overlap with the $(C_{60})^+(\text{CO}_2)_n$ signal. The insets a_1 and b_1 show fitted ion distribution curves of different species in the mass range of $(C_{60})^+(\text{CO}_2)_{44}$ (a_1) and $(C_{60})^-(\text{CO}_2)_{34}$ as interpreted by our evaluation software IsotopeFit²⁶.

We approached the interpretation of these anomalous spectral features by means of computations, both with DFT and molecular dynamics (MD) simulations. To gain insight into the interactions of a single CO_2 molecule with C_{60} , C_{60}^+ and C_{60}^- , DFT computations were performed. Some of the preferred optimized structures together with their geometrical parameters are shown in Figure 2. Equilibrium dissociation energies (D_e , also referred to as adsorption energies) are recorded in Table 1. Equilibrium refers to optimized geometries for both

the compound and the dissociated products. We also show the dissociation energies (D_{MD}) calculated with the classical force field used in the MD calculations for DFT optimized geometries. As can be expected for shallow potential energy surfaces and the harmonic approximation for vibrational frequency calculations, not all structures in Table 1 are true local minima if no symmetry constraints are present. For example, the vertical orientations over pentagons and hexagons on neutral C_{60} correspond to transition structures of 2nd ($N_f = 2$) and 3rd ($N_f = 3$) order respectively. With the addition of diffuse basis functions for anion frequency calculations could not be finished, even though the optimizations converged, so that for anions the reported structures might not be true minima. Although the computed adsorption energy of a single CO_2 molecule is slightly higher for anions than for cations, in this work we show that the CO_2 -adsorption capacity in the first adsorption shell is higher for cations than for anions due to steric effects.

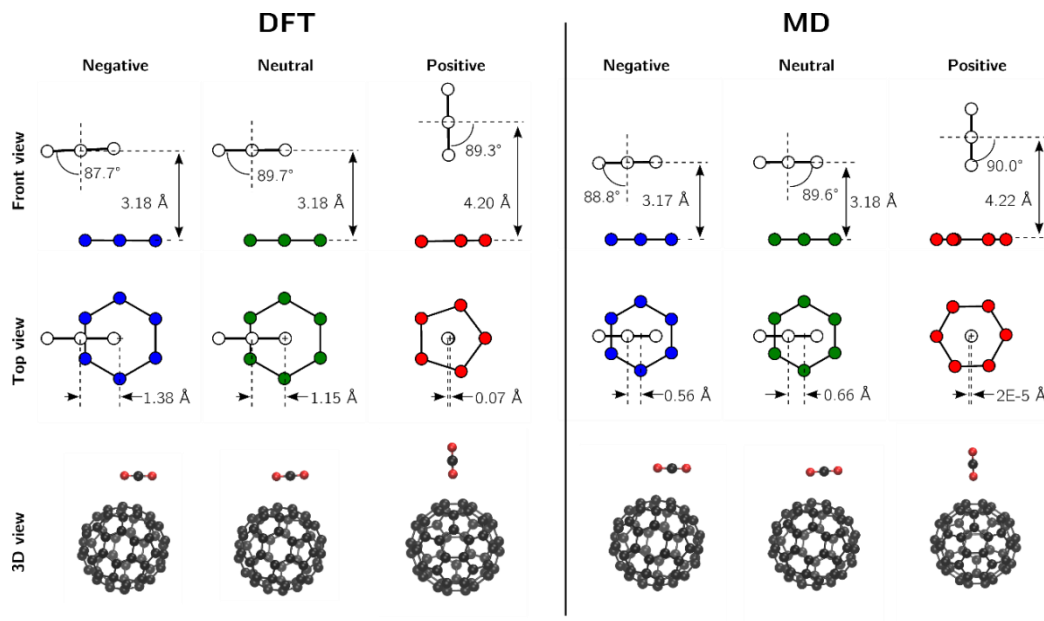


Figure 2. Front and top views of the three preferred orientations of a single CO_2 molecule adsorbed on C_{60}^- , C_{60} and C_{60}^+ as indicated by DFT and MD calculations.

Table 1. Total energies for the adsorption of a single CO₂ molecule on C₆₀, C₆₀⁺ and C₆₀⁻ from DFT calculations. The preferred structures shown in Figure 2 are highlighted.

	q/e	basis	site	orien	T/eV	ZP/eV	N _f	CP/eV	D _e /eV	D ₀ /eV	D _{CP} /eV	D _{MD} /eV
C ₆₀	0	6-31g(d)			-62190.423	10.435						
C ₆₀	1	6-31g(d)			-62182.757	10.354						
C ₆₀	-1	6-31g(d)			-62193.698							
CO ₂	0	6-31g(d)			-5129.890	0.322						
CO ₂	0	6-31g+(d)			-5130.079	0.321						
C₆₀CO₂	0	6-31g(d)	hex	flat	0 (-67320.4330)	10.759	0	0.050	0.120	0.118	0.070	0.100
C ₆₀ CO ₂	0	6-31g(d)	pent	flat	0.010	10.762	0		0.109			0.094
C ₆₀ CO ₂	0	6-31g(d)	pent	vert	0.066		2		0.054			0.054
C ₆₀ CO ₂	0	6-31g(d)	hex	vert	0.074		3		0.046			0.060
C₆₀CO₂	1	6-31g(d)	pent	vert	0 (-67312.7744)	10.700	0	0.029	0.127	0.103	0.098	0.083
C ₆₀ CO ₂	1	6-31g(d)	hex	vert	0.002	10.692	0	0.029	0.125	0.109	0.096	0.090
C ₆₀ CO ₂	1	6-31g(d)	hex	flat	0.015		1		0.112			0.076
C ₆₀ CO ₂	1	6-31g(d)	pent	flat	0.015	10.695	0		0.112			0.072
C₆₀CO₂	-1	6-31g+(d)	hex	flat	0 (-67323.9386)			0.028	0.162		0.134	0.119
C ₆₀ CO ₂	-1	6-31g+(d)	pent	flat	0.025				0.136			0.109
C ₆₀ CO ₂	-1	6-31g+(d)	pent	vert	0.104				0.057			0.023
C ₆₀ CO ₂	-1	6-31g+(d)	hex	vert	0.113				0.049			0.031

q	Charge
T	Total energy or relative energy
ZP	Zero point correction
N _f	Number of imaginary frequencies (0: local minimum, >0: transition structures)
CP	Counterpoise correction
D _e (eV)	dissociation energy from uncorrected total energies
D ₀ (eV)	dissociation energy from zero point corrected energies
D _{CP} (eV)	dissociation energy from counterpoise corrected energies
D _{MD} (eV)	dissociation energy from force field of DFT optimized geometries
site	adsorption site
orien	orientation of CO ₂ in the optimized structure

The results summarized in Table 1 indicate that hexagons are preferred over pentagons as adsorption sites for C_{60} and C_{60}^- . The situation is more complex for C_{60}^+ with an only slight preference for hexagonal sites if zero-point correction is taken into account (D_0). Horizontal adsorption is preferred on C_{60} and C_{60}^- by 0.06 eV or more, while vertical adsorption is preferred on C_{60}^+ . These preferences can be understood in terms of the relatively positive carbon center (+ 0.76 e in terms of Mulliken charges) and negative oxygen ends of the CO_2 molecule (- 0.38 e). The energy difference between the vertical and horizontal configuration (without any corrections) is only 14.5 meV for the cation (vertical preferred), 104 meV for the anion (horizontal preferred), and for the neutral 66 meV (horizontal preferred). The adsorbed CO_2 is slightly bent (177.8°) in the case of the anionic complex. Mulliken charges imply that CO_2 becomes slightly polar upon adsorption on $C_{60}^{+,0,-}$ and a small amount of charge is transferred to the fullerene (< 0.2 e). The charge transfer due to CO_2 adsorption on C_{60} is visualized in Figure 3 for (a) the cation (b) the neutral (c) the anion. A completely different scheme for charge accumulation (red) and depletion (blue) is observed for the cation and the anion and the induced polarity of CO_2 can be clearly seen in panel (a). Note that the isovalues of the three surfaces per panel are small (± 0.0001 , ± 0.0002 , ± 0.0004 a.u.) because the overall charge transfer is also rather small. In bare C_{60}^- the additional charge is distributed over the whole fullerene (not shown) and resembles the LUMO molecular orbital of C_{60} .

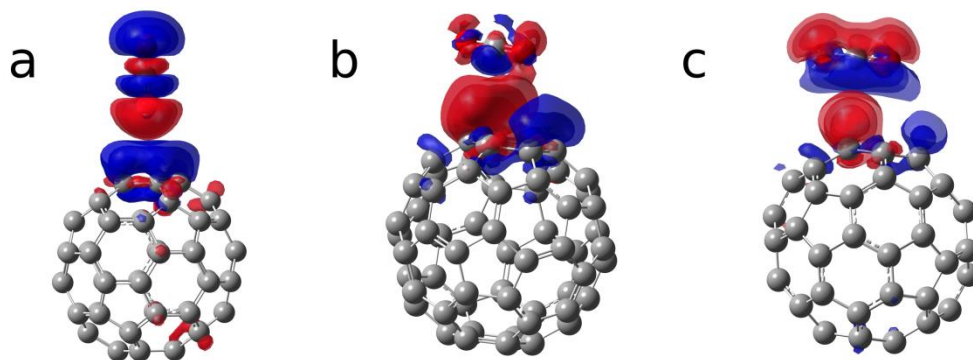


Figure 3: Charge accumulation (red colors) and depletion (blue colors) due to CO₂ adsorbed on (a) C₆₀⁺, (b) C₆₀, (c) C₆₀⁻. Surfaces of the charge density difference $\rho(\text{C}_{60}\text{CO}_2^{+,0,-}) - \rho(\text{C}_{60}^{+,0,-}) - \rho(\text{CO}_2)$ for isovalues of ± 0.0001 , ± 0.0002 , and ± 0.0004 (atomic units) are shown.

The computed binding energies and binding modes can be compared with previously published results for CO₂ adsorption on carbonaceous materials. In the classical model of Arab et al. CO₂ adsorbs horizontally on external sites of a single walled nanotube (SWNT) bundle with a binding energy of 0.113 eV¹². This binding energy is very close to our estimate of 0.120 eV on neutral C₆₀. The energy induced by carbon polarizability can be neglected¹². The CO₂ dimer interaction energy on SWNT bundles lies between 55 and 64 meV depending on the adsorption site. A parallel, slightly shifted configuration was found except for interstitial sites. In MP2/AVTZ calculations adsorption energies of 0.117 eV on graphite and 0.113 eV on a (9,0) nanotube exceed the experimental heat of adsorption of 0.024 eV in SWNTs¹¹. As in our results for neutral C₆₀, CO₂ favors the horizontal adsorption above the center of a C₆ ring. On neutral C₆₀ a CO₂ adsorption energy of only 0.037 eV was reported employing GGA/PBE density functional theory without dispersion correction. However, the optimized geometry resembles our results. Gao et al. also showed that adsorption can be enhanced by calcium doping⁷.

Another GGA/PBE calculation yielded a binding energy of 0.400 eV for CO₂ adsorbed on graphene at a distance of 3.0 Å. The vertical configuration adsorbs only with 0.294 eV²⁷. In plane-wave DFT CO₂ adsorbs on graphene nanoribbons with 0.31 eV binding energy¹⁰. On SWNTs LDA/PW calculations yielded adsorption energies between 0.089 and 0.109 eV with CO₂ positioned between 3.23 and 3.54 Å above hexagons²⁸. Reactions pathways of the dissociative adsorption of CO₂ on graphite were investigated by Xu et al.⁸ A smallest barrier of

5.17 eV was found for dissociative adsorption of a single oxygen atom. The reaction is endothermic with 4.2 eV. A combined experimental and theoretical study of CO₂ chemisorption on carbonaceous surfaces revealed a first region of high and decreasing adsorption energy and a second region of high coverage, where the adsorption energy stabilizes in the range of 0.217-0.39 eV²⁹.

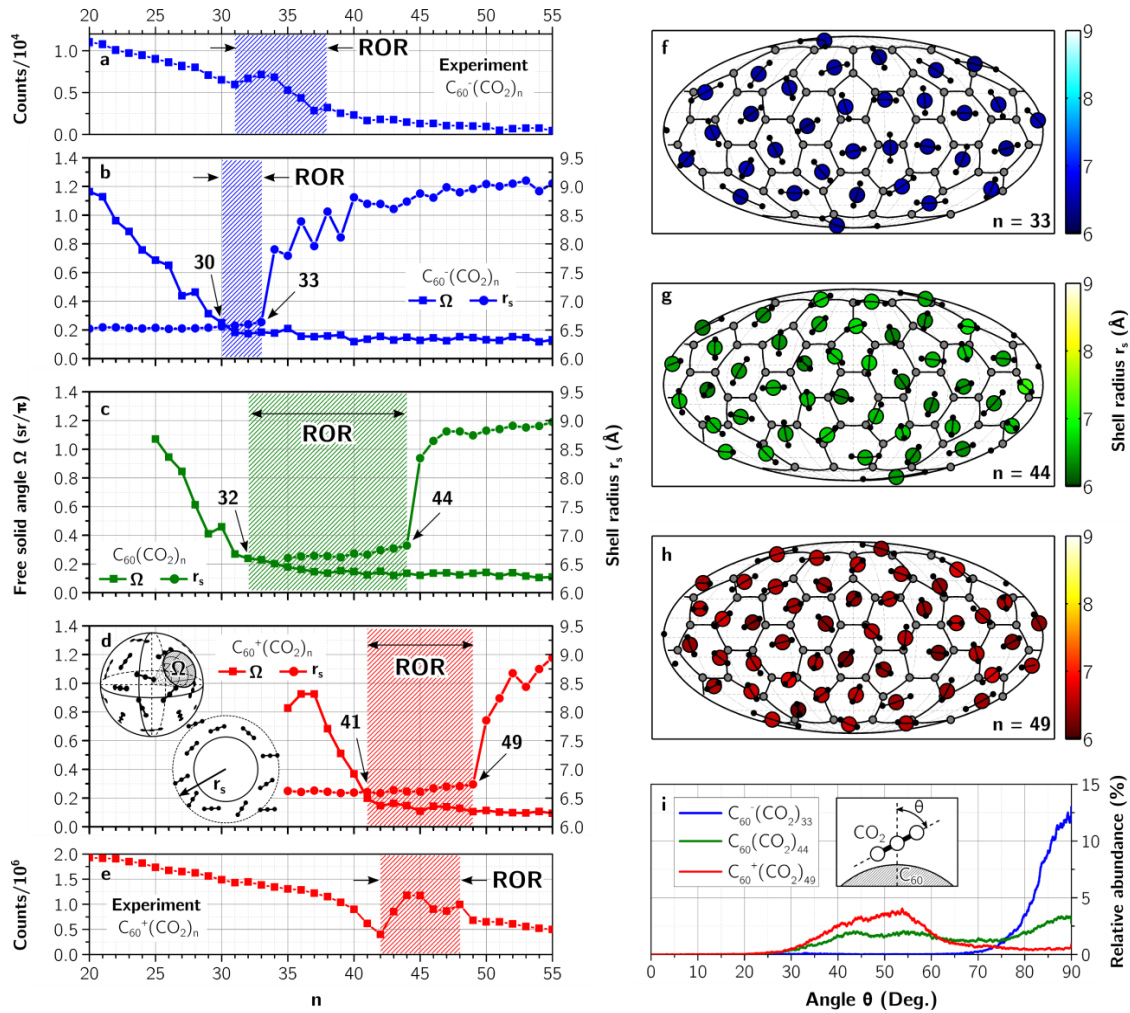


Figure 4: Ion yield measurements in the region of the first shell closure (a, e) and results from MD simulations (b - d, f - i). The positions of the CO₂s on the C₆₀ and their angles in the case of full coverage are shown in f-i.

The results of our MD simulations provide atomistic insight into the CO₂ layers on neutral cationic and anionic C₆₀ with respect to the number of molecules in the first shell and their orientation. To assess the CO₂ capacity in the first shell, we computed the “shell radius” as the smallest sphere within which a given number of adsorbed CO₂ molecules resides (Figure 4 b-d, f-h). With this approach, we find 33, 44 and 49 CO₂ molecules to reside within the first shell for negative, neutral and positive C₆₀, respectively. Relative to neutral C₆₀, the “storage capacity” in the first shell therefore decreases by 25% for the C₆₀ anions and increases by about 10% for its cations. The shell closures for the cation at $n = 48$ (49 in the MD simulation) and for the anion at $n = 38$ (33 in the MD simulation) are visible in the experimental results shown in Figure 4e and 4a respectively. As expected from our experience, the MD simulations only give qualitatively reasonable results for the anionic case.

Surface diagrams for fully covered neutral and ionic C₆₀, together with the angular distribution functions are shown in Figure 4 f-i. Striking differences in the orientational distributions can be seen which can be explained by the quadrupole moment of the CO₂ molecule. Electrostatic interaction between the positive carbon center and a negatively charged C₆₀ favors a flat orientation for the CO₂ molecules. On the other hand, the electrostatic interaction between the negative terminal O atoms in CO₂ (or the combined negative charge of the split charges for oxygen in the model of Murthy³⁰ in the MD simulations) and a positively charged C₆₀ favors a tilted orientation, with CO₂ standing up by 40-60 degrees. In neutral C₆₀ the alignment of CO₂ shows an intermediate behavior. These angular distributions do not completely resemble the DFT/MD results for single CO₂ adsorption (perfectly vertical/flat) because of the intermingling CO₂-CO₂ intermolecular interactions.

An interesting feature was observed in the simulations when looking at the CO₂-free solid angle Ω . Omega is defined as the largest possible opening angle in steradians of a cone that has its top in the center of the fullerene and does not contain any centers of the adsorbed CO₂ atoms. For different coverage numbers for the three charge states of C₆₀ we saw a “bald spot” ($\Omega \gg 0$) that dissipates with increasing coverage numbers in each case (Figure 4 b-d). Figure 5 shows the formation and evolution of this bald spot on charged and neutral C₆₀. Clearly, in each case, the bald spots fill out with increasing CO₂ adsorption until the surface is fully covered. Then several more molecules fit into the first shell before a second layer begins to form (i.e. full coverage is possible over a certain range of n before a second layer starts to form). In between there is a “region of rearrangement” (ROR: $\Omega < \pi/4$, $r_s < 7\text{\AA}$) in which the first shell molecules change their positions and angles. This region is highly charge-dependent and is revealed in the experiment as a broad anomaly in the cluster size distribution rather than a sharp peak (Figure 4a and 4e).

In the simulations, the free solid angle Ω almost vanishes at a coverage of $n = 30$ for the anion and $n = 41$ for the cation. Thus the first minima in the experimental data at $n = 31$ for the anion and $n = 42$ for the cation are interpreted as the closure of the bald spot. The simulations also show that C₆₀ is fully covered within a certain range of n (30 to 33 for the anion, 41 to 49 for the cation) due to CO₂ rearrangement without starting a second adsorption shell. Thus the last anomalies in the ion yield (the right end of the region of rearrangement ROR) at $n = 38$ (anion) and $n=48$ (cation) are interpreted as complete closure of the first adsorption shell. Note that the simulations for the anion predict a much narrower ROR than observed in the experiment, which might be an artifact of the force field or of the fixed charge distribution. However, DFT calculations of MD optimized structures revealed a surprisingly homogeneous distribution of the additional electron of C₆₀⁻ that resembles the lowest unoccupied orbital of C₆₀.

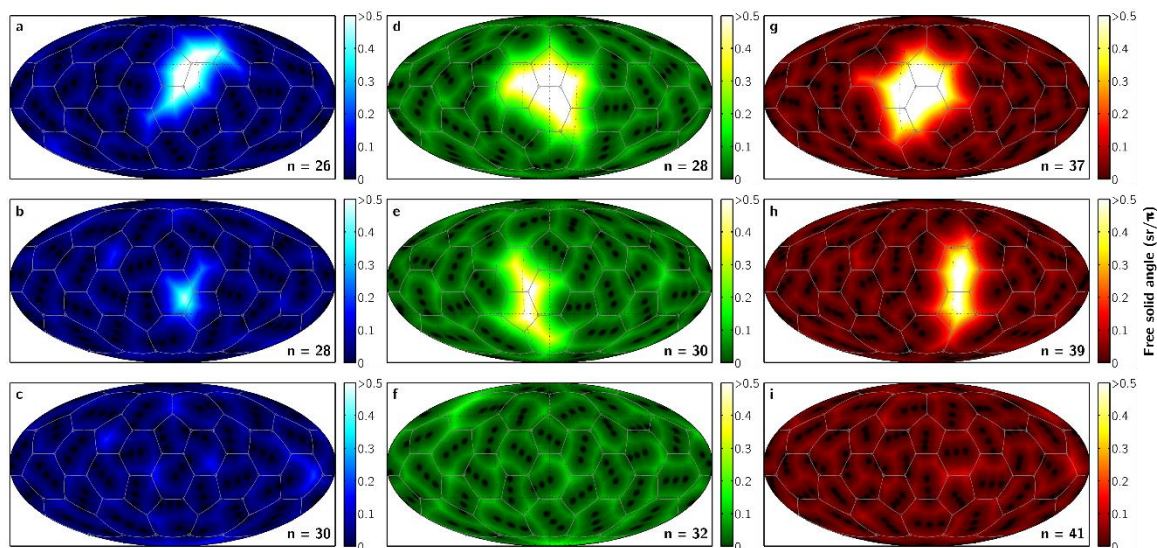


Figure 5. Computed CO_2 -free solid angle on negatively (a-c), neutral (d-f) and positively (g-i) charged C_{60} surface showing the formation of a bald spot and its dissipation for increasing coverage number n of CO_2 molecules.

Our attempts to understand our experimental results with the application of DFT and MD simulations have provided a vivid picture of the step-by-step coverage of C_{60} , C_{60}^+ and C_{60}^- . The electronic properties of CO_2 have decisive consequences for the nature of the adsorption as the captured CO_2 molecules respond to the absence or presence of charge (positive or negative) on the C_{60} surface. An unambiguous charge order in CO_2 adsorption *capacity* was clearly observed experimentally for the first time. Our computations have allowed us to understand this charge order in terms of the orientation of the CO_2 molecules on the charged carbonaceous surface that results from the electrostatic interaction between the charge on the surface and the quadrupole of CO_2 . This orientation effect in the presence of charge is expected to apply generally to adsorption on other charged carbonaceous surfaces, and to surfaces in general, and so to control (enhance or diminish) the capture of CO_2 by adsorption.

Computational details

The energetics and geometries of neutral, cationic, and anionic $C_{60}CO_2$ structures were calculated by means of density functional theory (DFT). All structures were fully optimized without constraints in order to account for the slight deformation of fullerene and of CO_2 arising from each in the presence of the other. Configurations for the adsorption of a single CO_2 molecule were optimized, starting from five different initial geometries with OCO flat (two centered over a hexagon (hex), three over a pentagon (pent)) and two initial geometries (one centered over a hexagon, one over a pentagon) for CO_2 vertical (vert) adsorption. The calculations were performed with the GAUSSIAN 09 program³¹ with the ω B97X-D dispersion corrected hybrid density functional^{32, 33} and the 6-31g(d) basis set^{34, 35} with additional diffuse functions (+) for anions³⁶. We found this density functional to be among the best long-range corrected ones³⁷ in previous studies on the adsorption of H_2 , CH_4 and C_2H_4 on fullerenes¹⁹⁻²².

MD-simulations were performed to provide structural insight into the observed states of physisorption. Non-polarizable CO_2 and C_{60} were kept rigid using the quaternion propagation formalism. We used parameters from Martínez-Alonso et al.³⁸ for C_{60} - CO_2 forces and added a distributed charge of ± 1 e on the fullerene ions. The charge primarily resides on the fullerene because of its low ionization energy (7.6 eV)¹⁹ and its high electron affinity (2.6 eV)³⁹ compared to CO_2 (13.78 and - 0.6 eV respectively)²⁵. Mulliken partial charges from the DFT calculations sum up to 0.95 e on C_{60} for cationic $C_{60}CO_2$ and -1.20 e on C_{60} for anionic $C_{60}CO_2$. The charge distributions of the missing/additional electron resemble the HOMO/LUMO molecular orbitals of C_{60} also for higher CO_2 occupations. The small, but non-negligible, influence due to the quadrupole moment of the CO_2 adsorbates on the charge distribution cannot be reflected in our MD-simulations. However, the similarities in energetic order (Table 1) and

optimized geometries between DFT and MD (Figure 2) results indicate that the model adopted for anions and cations is capable of reproducing the major adsorption features of charge dependent adsorption capacity.

For the CO₂-CO₂ interaction, we used a 5-charge model (a split charge for each oxygen 0.1216 e/-0.6418 e and one site centered at carbon with 1.0404 e) developed by Murthy et al.³⁰ that has been used previously to simulate CO₂ clusters in vacuum^{40, 41}. After initializing a randomly distributed dilute cloud of CO₂ molecules around C₆₀, the computational procedure consisted of two steps: First, the system was heated to temperatures of 120 K and cooled down again within a total simulation time of 50 ps. Second, the energy was locally optimized with a trust-region optimization algorithm. The annealing towards much higher temperatures than in the experiment guarantees a better sampling of the potential energy surface in finding distinct initial geometries for the local optimizer.

In order to find geometries with low total configuration energy, we inspected a large number of such simulations for each cluster (2500 to 4000, depending on the cluster size). However, due to the size of the system and the huge configurational space, global minima were only reached with very few CO₂ adsorbate molecules, so that dissociation energies for larger clusters could not be obtained reliably and were not reported in this work.

Angular distributions were obtained from the CO₂ coordinates at all integration steps during the cooling process of longer simulations (200 ps in total with a time step of 500 fs) with lower annealing temperatures (50K to 80K in steps of 10K). For a representation of the shell radius we used the distance between the C₆₀ center of mass and the closest atom of the outermost CO₂ molecule. We searched for the smallest shell radius in all simulations and integration steps for a given cluster size.

Structures were simulated and optimized with our own code that is specialized for simulations and structure optimizations of clusters in vacuum with flexible force fields and fast automation and data analysis.

Experimental details

The experimental setup has been described in detail elsewhere^{42, 43}. In brief, helium (purity 99.9999%) is cooled to 9.5K by a closed cycle two-stage cryocooler (SRDK-415D-F50H, Sumitomo Heavy Industries Ltd.). Helium nanodroplets are formed by helium expansion at a stagnation pressure of 2.0 MPa through a 5 μm nozzle into vacuum. Under these conditions the estimated average number of helium atoms per droplet is in the order of 5×10^5 . The droplets are superfluid with a temperature of 0.37K⁴⁴. After formation, the helium droplet beam passes a 0.8 mm conical skimmer to avoid shock waves and enters a differentially pumped pickup chamber. The pickup chamber is again divided into two differentially pumped regions. A small amount of C₆₀ (SES research, purity 99.95%) is vaporized into the first region from a heated crucible. In the second region CO₂ (Messer; purity 99.9995%) is introduced from an external reservoir and fed into the chamber with a flow controller. Stable and efficient pickup conditions are achieved at a constant source temperature of 330 °C for C₆₀ and 2 mPa for CO₂. After the pickup process the He beam enters the ionization chamber and is crossed with an electron beam of 8.5 eV and 120 eV for the optimum production of anions and cations, respectively. The resulting anions and cations are guided by a weak electrostatic field toward the entrance of a time-of-flight mass spectrometer. The commercial orthogonal reflectron time-of-flight mass spectrometer (Tofwerk) separates the masses and achieves a mass resolution of $R \sim 5000\text{FWHM}$ (in V-mode). Ultimately the ions are detected by a multi-channel plate operated in a single counting mode.

The evaluation of the raw mass spectra was performed with our own software IsotopeFit, which is able to extract the abundances of all peaks in the spectrum by fitting the ion distribution curves of all species that contribute to the signal ²⁶. The insets in Figure 1 show the raw spectra for $C_{60}^-(CO_2)_{34}$ and $C_{60}^+(CO_2)_{44}$ together with the fitted ion distribution curves in the corresponding mass range as an example. Please note the slightly different curves of the raw spectra in Figure 1 and the extracted total counts per ion in Figure 4a and 4e which stems from overlapping ion signals as well as area distortions due to isotopic effects which are eliminated by summation over the fitted signals for contributing isotopes.

Acknowledgements

This work was given financial support by the Austrian Science Fund (FWF), Wien (P26635, and I978). This work was supported by the Austrian Ministry of Science BMWF as part of the UniInfrastrukturprogramm of the Focal Point Scientific Computing at the University of Innsbruck.

1. T. A. Steriotis, K. L. Stefanopoulos, F. K. Katsaros, R. Gläser, A. C. Hannon and J. D. F. Ramsay, *Phys. Rev. B*, 2008, **78**, 115424.
2. O. Shekhah, Y. Belmabkhout, Z. Chen, V. Guillerm, A. Cairns, K. Adil and M. Eddaoudi, *Nat. Comm.*, 2014, **5**, 4228.
3. B. K. Chang, P. D. Bristowe and A. K. Cheetham, *Phys Chem Chem Phys*, 2013, **15**, 176-182.
4. J. Kim, L.-C. Lin, J. A. Swisher, M. Haranczyk and B. Smit, *J. Am. Chem. Soc.*, 2012, **134**, 18940-18943.
5. I. Matito-Martos, A. Martin-Calvo, J. J. Gutierrez-Sevillano, M. Haranczyk, M. Doblare, J. B. Parra, C. O. Ania and S. Calero, *Phys Chem Chem Phys*, 2014, **16**, 19884-19893.
6. T. Rodenas, I. Luz, G. Prieto, B. Seoane, H. Miro, A. Corma, F. Kapteijn, F. X. Llabrés i Xamena and J. Gascon, *Nat. Mater.*, 2015, **14**, 48-55.
7. B. Gao, J.-x. Zhao, Q.-h. Cai, X.-g. Wang and X.-z. Wang, *J. Phys. Chem. A*, 2011, **115**, 9969-9976.
8. S. C. Xu, S. Irle, D. G. Musaev and M. C. Lin, *J. Phys. Chem. B*, 2006, **110**, 21135-21144.
9. T. T. Trinh, D. Bedeaux, J. M. Simon and S. Kjelstrup, *Phys Chem Chem Phys*, 2015, **17**, 1226-1233.

10. B. Huang, Z. Li, Z. Liu, G. Zhou, S. Hao, J. Wu, B.-L. Gu and W. Duan, *J. Phys. Chem. C*, 2008, **112**, 13442-13446.
11. M. Cinke, J. Li, C. W. Bauschlicher, A. Ricca and M. Meyyappan, *Chem. Phys. Lett.*, 2003, **376**, 761-766.
12. M. Arab, F. Picaud, M. Devel, C. Ramseyer and C. Girardet, *Phys. Rev. B*, 2004, **69**, 165401.
13. M. Bienfait, P. Zeppenfeld, N. Dupont-Pavlovsky, M. Muris, M. R. Johnson, T. Wilson, M. DePies and O. E. Vilches, *Phys. Rev. B*, 2004, **70**, 035410.
14. D. Mantzalis, N. Asproulis and D. Drikakis, *Phys. Rev. E*, 2011, **84**, 066304.
15. Q. Sun, Z. Li, D. J. Searles, Y. Chen, G. Lu and A. Du, *J. Am. Chem. Soc.*, 2013, **135**, 8246-8253.
16. H. Guo, W. Zhang, N. Lu, Z. Zhuo, X. C. Zeng, X. Wu and J. Yang, *J. Phys. Chem. C*, 2015, **119**, 6912-6917.
17. T. T. Trinh, T. J. H. Vlugt, M.-B. Hägg, D. Bedeaux and S. Kjelstrup, *Energy Procedia*, 2015, **64**, 150-159.
18. Y. Jiao, Y. Zheng, S. C. Smith, A. Du and Z. Zhu, *ChemSusChem*, 2014, **7**, 435-441.
19. A. Kaiser, C. Leidlmair, P. Bartl, S. Zöttl, S. Denifl, A. Mauracher, M. Probst, P. Scheier and O. Echt, *J. Chem. Phys.*, 2013, **138**, 074311-074313.
20. S. Zöttl, A. Kaiser, M. Daxner, M. Goulart, A. Mauracher, M. Probst, F. Hagelberg, S. Denifl, P. Scheier and O. Echt, *Carbon*, 2014, **69**, 206-220.
21. S. Zöttl, A. Kaiser, P. Bartl, C. Leidlmair, A. Mauracher, M. Probst, S. Denifl, O. Echt and P. Scheier, *J. Phys. Chem. Lett.*, 2012, **3**, 2598-2603.
22. A. Kaiser, S. Zöttl, P. Bartl, C. Leidlmair, A. Mauracher, M. Probst, S. Denifl, O. Echt and P. Scheier, *ChemSusChem*, 2013, **6**, 1235 – 1244.
23. C. Leidlmair, Y. Wang, P. Bartl, H. Schöbel, S. Denifl, M. Probst, M. Alcamí, F. Martín, H. Zettergren, K. Hansen, O. Echt and P. Scheier, *Phys. Rev. Lett.*, 2012, **108**, 076101.
24. A. Mauracher, A. Kaiser, M. Probst, S. Zöttl, M. Daxner, J. Postler, M. M. Goulart, F. Zappa, D. K. Bohme and P. Scheier, *Int. J. Mass. Spectrom.*, 2013, **354–355**, 271-274.
25. Computation Chemistry and Benchmark DataBase of the National Institute of Standards and Technology, <http://cccbdb.nist.gov/>, Accessed 2015/01/15.
26. S. Ralser, J. Postler, M. Harnisch, A. M. Ellis and P. Scheier, *Int. J. Mass. Spectrom.*, 2015, **379**, 194-199.
27. A. Ghosh, K. S. Subrahmanyam, K. S. Krishna, S. Datta, A. Govindaraj, S. K. Pati and C. N. R. Rao, *J. Phys. Chem. C*, 2008, **112**, 15704-15707.
28. Z. Jijun, B. Alper, H. Jie and L. Jian Ping, *Nanotechnology*, 2002, **13**, 195.
29. A. Montoya, F. Mondragón and T. N. Truong, *Carbon*, 2003, **41**, 29-39.
30. C. S. Murthy, S. F. O'Shea and I. R. McDonald, *Mol. Phys.*, 1983, **50**, 531-541.
31. M. J. Frisch, G. W. Trucks, H. B. Schlegel, G. E. Scuseria, M. A. Robb, J. R. Cheeseman, G. Scalmani, V. Barone, B. Mennucci, G. A. Petersson, H. Nakatsuji, M. Caricato, X. Li, H. P. Hratchian, A. F. Izmaylov, J. Bloino, G. Zheng, J. L. Sonnenberg, M. Hada, M. Ehara, K. Toyota, R. Fukuda, J. Hasegawa, M. I. a. T., Nakajima, Y. Honda, O. Kitao, H. Nakai, T. Vreven, J. Montgomery, J. A. , J. E. Peralta, F. Ogliaro, M. Bearpark, J. J. Heyd, E. Brothers, K. N. Kudin, V. N. Staroverov, R. Kobayashi, J. Normand, K. Raghavachari, A. Rendell, J. C. Burant, S. S. Iyengar, J. Tomasi, M. Cossi, N. Rega, J. M. Millam, M. Klene, J. E. Knox, J. B. Cross, V. Bakken, C. Adamo, J. Jaramillo, R. Gomperts, R. E. Stratmann, O. Yazyev, A. J. Austin, R. Cammi, C. Pomelli, J. W. Ochterski, R. L. Martin, K. Morokuma, V. G. Zakrzewski, G. A. Voth, P. Salvador, J. J. Dannenberg, S. Dapprich, A. D. Daniels, Ö. Farkas, J. B. Foresman, J. V. Ortiz, J. Cioslowski and D. J. Fox, *Gaussian Inc. Wallingford CT 2009*.
32. S. Grimme, *J. Comp. Chem.*, 2006, **27**, 1787-1799.
33. J.-D. Chai and M. Head-Gordon, *Phys. Chem. Chem. Phys.*, 2008, **10**, 6615-6620.

- 34. R. Ditchfield, W. J. Hehre and J. A. Pople, *J. Chem. Phys.*, 1971, **54**, 724-728.
- 35. W. J. Hehre, R. Ditchfield and J. A. Pople, *J. Chem. Phys.*, 1972, **56**, 2257-2261.
- 36. T. Clark, J. Chandrasekhar, G. W. Spitznagel and P. V. R. Schleyer, *J. Comput. Chem.*, 1983, **4**, 294-301.
- 37. J. Klimes and A. Michaelides, *J. Chem. Phys.*, 2012, **137**, 120901.
- 38. A. Martínez-Alonso, J. M. D. Tascón and E. J. Bottani, *J. Phys. Chem. B*, 2000, **105**, 135-139.
- 39. O. V. Boltalina, L. N. Sidorov, A. Ya. Borshchevsky, E. V. Sukhanova and E. V. Skokan, *Rapid Communications in Mass Spectrometry*, 1993, **7**, 1009-1011.
- 40. J.-B. Maillet, A. Boutin, S. Buttefey, F. Calvo and A. H. Fuchs, *J. Chem. Phys.*, 1998, **109**, 329-337.
- 41. J.-B. Maillet, A. Boutin and A. H. Fuchs, *J. Chem. Phys.*, 1999, **111**, 2095-2102.
- 42. L. An der Lan, P. Bartl, C. Leidlmair, H. Schöbel, R. Jochum, S. Denifl, T. D. Märk, A. M. Ellis and P. Scheier, *J. Chem. Phys.*, 2011, **135**, 044309.
- 43. H. Schöbel, P. Bartl, C. Leidlmair, S. Denifl, O. Echt, T. D. Märk and P. Scheier, *Eur. Phys. J. D*, 2011, **63**, 209-214.
- 44. J. P. Toennies and A. F. Vilesov, *Angew. Chem. Int. Ed.*, 2004, **43**, 2622-2648.